

## GAMMA-RAY BURSTS WITH CONTINUOUS ENERGY INJECTION AND THEIR AFTERGLOW SIGNATURE

BING ZHANG &amp; PETER MÉSZÁROS

Astronomy &amp; Astrophysics Dept., Pennsylvania State University, University Park, PA 16803

*Accepted for publication in The Astrophysical Journal*

## ABSTRACT

We consider generically the problem of a Gamma-ray burst (GRB) fireball with an additional energy injection, either in the form of a Poynting-flux-dominated outflow or a kinetic-energy-dominated matter shell injected after the burst. Generally, a total injection energy comparable to that of the impulsive energy in the initial fireball is required to make a detectable signature in the afterglow lightcurves. When this criterion is met in the case of Poynting-flux-dominated injection, this leads to a gradual achromatic bump appearing in the otherwise power-law afterglow lightcurve. Alternatively, in the case when the injection is kinetic-energy-dominated, the results depend on whether the collision between the rear (injected) and the forward shell is mild or violent. If the relative velocity between the colliding shells does not exceed a critical value defined by their energy ratio, the collision is mild, and the injection may be analogous to the Poynting-flux injection case. Otherwise, the injection is violent, and an additional pair of shocks will form at the discontinuity between two colliding shells, so that there are altogether three shock-heated regions from which the emission contributes to the final lightcurves. We describe the shell-merging process in detail including collision and relaxation by taking into account the dynamical evolution and the emission from the various shocks involved. Assuming synchrotron emission, we calculate afterglow lightcurves in the X-ray, optical and radio bands for the various cases. The injection signatures due to violent matter-dominated collisions are abrupt and complicated, due to the emission from any of the three emitting regions, and depending on the injection parameters and the observed energy bands. This differs from the gradual bump signature found in the Poynting-flux injection case. In both the Poynting-flux-dominated and the kinetic-energy-dominated cases, the energetics of the fireball as well as the absolute afterglow flux level after the injection are boosted with respect to the one without post-burst injection. Identifying the different injection signatures from future early afterglow observations may provide diagnostics about the nature of the fireball and of the central engine.

*Subject headings:* gamma rays: bursts - radiation mechanisms: non-thermal - shock waves - stars: magnetic fields

## 1. INTRODUCTION

Classical Gamma-ray burst (GRB) afterglow models generally invoke an “impulsively” injected (possibly collimated) fireball running into an ambient interstellar medium (ISM) or into a pre-burst stellar wind. In principle, after the initial fireball starts to decelerate, additional injection of energy is still possible. There are at least three motivations to study the post-burst injection possibility more carefully. 1: Additional injection is a natural expectation of the internal shock GRB model, which predicts that some slow shells will trail the outermost fast shell and run into it when the latter is decelerated (e.g. Rees & Mészáros 1998; Kumar & Piran 2000). In some cases, the central engine may also inject fast shells at a later time. Later injection is also naturally expected in certain types of the central engine models (e.g. Dai & Lu 1998; Zhang & Mészáros 2001a). 2: A GRB fireball can in principle be dominated by the kinetic energy of the baryons or by a Poynting-flux component. Any clue about the fireball nature is presently lacking. As discussed below, an injection signature in the GRB lightcurve may directly provide diagnostics about the nature of the injection as well as information about the central engine. 3: “Bump” features have been observed in several GRB afterglows (e.g. GRB 970228, GRB 970508, GRB 980326, GRB 000103C, etc.).

and various interpretations have been proposed, e.g., refreshed shocks (Panaitescu, Mészáros & Rees 1998), supernova components (Bloom et al. 1999; Reichart 1999; Galama et al. 2000), dust echos (Esin & Blandford 2000), and gravitational micro-lensing events (Garnavich, Loeb & Stanek 2000). It would be of great interest to study the injection feature in more detail to find distinct properties to be differentiated from other interpretations. Such injections are likelier to occur in the early afterglow phase. The planned future broad-band GRB mission *Swift* will have the ability of recording broadband early afterglow signals from many GRBs, and thus bring unique opportunities to study the injection features.

Depending on the different types of the central engine, the post-injection could consist of, e.g., some kinetic-energy (i.e. baryon) dominated shells, or a Poynting-flux-dominated wind (Usov 1994; Mészáros & Rees 1997b). Here we present a generic study on various injection cases. Generally speaking, an injection energy comparable to the initial impulsive energy is required to make the injection noticeable. We therefore study a system containing an impulsive shell which is already heated during the shell-ISM interaction, and which is collecting material from the ISM, and in the meantime also receives a large enough injection energy from a continuous Poynting wind or a trailing matter shell. We first discuss in §2 the simplest case, in which

the fireball continuously receives pure energy with negligible baryon loading, very likely in the form of Poynting flux. Since no reverse shock is expected in such a case, the injection signature is solely from the forward shock emission, through the change of the blastwave global dynamics. In §3, we discuss the more complicated matter shell injection case. In real situations, shell collisions may occur more than once. Here we only investigate the detailed physics of one such post-collision. The same analysis, when applied several times, is generic in delineating the more complicated multi-collision cases. We first analyze the general hydrodynamics of the three-shell (impulsive shell, injective shell, and ISM) interaction (§3.1). After reviewing the general shell evolution history, we solve numerically for the condition of a “violent injection”, in which an additional pair of strong shocks form at the discontinuity of the two colliding shells (§3.2). We then outline in §3.3 the hydrodynamics of the three-shell-interaction process in detail by dividing the whole process into five stages (§3.3.1-§3.3.5), namely (1) pre-collision; (2) mild injection; (3) violent injection; (4) relaxation; (5) post-relaxation. In §3.4, we discuss synchrotron radiation from all the possible shocked regions in various stages, and present the injection signatures in the broadband lightcurves. Our findings are summarized and discussed in §4.

## 2. INJECTION FROM A POYNTING-FLUX-DOMINATED FLOW

The conventional definition of a Poynting-flux-dominated flow is  $L_{\pm,\gamma,N}/L_P \ll 1$ , where  $L_{\pm,\gamma,N}$  is the luminosity of the electron-position pair, radiation and nucleon components, and  $L_P$  is the luminosity of the Poynting-flux (i.e. magnetic field) dominated outflow component (e.g. Usov 1999). In the context of GRBs, discussions of a Poynting-dominated flow as compared to a kinetic-energy-dominated flow are mainly focused on the paradigm of an approximately baryon-free Poynting flow, which are not as conducive to collisionless shock formation, so in this case GRBs may be powered by the non-linear breakdown of large-amplitude electromagnetic waves (Usov 1994; Blackman & Yi 1998; Lyutikov & Blackman 2001; for a review, see Usov 1999). However, in both scenarios, collisionless external forward shocks are believed to form in the afterglow phase (Usov 1999). Although the baryon free nature at the GRB prompt phase is uncertain (e.g. Spruit, Daigne & Drenkhahn 2001), in the later injection phase the baryon loading could be in principle much lower and the injection could be in the form of an almost baryon-free Poynting-flux-dominated wind. In such a case, no collisionless reverse shock is expected to propagate into the wind (Kennel & Coroniti 1984, Usov 1999; essentially, because the sound speed in the ejecta is close to the speed of light), and the injection energy is used to increase the total energetics of the fireball.

Considering an adiabatic relativistic hot shell which is collecting material as it expands into the ISM and which receives an energy input from the central engine via a Poynting-flux-dominated flow, the differential energy conservation equation in a fixed frame is  $d[\Gamma(M_0c^2 + M_2c^2 + U)] = dM_2c^2 + dE_{\text{inj}}$ , where  $M_0$ , and  $M_2$  are the masses of the impulsive shell and the swept-up ISM, respectively<sup>1</sup>,

$E_{\text{inj}}$  is the received injection energy, and  $\Gamma$  is the bulk Lorentz factor of the blastwave. The injection wind can be approximated as being cold, so it does not provide any internal energy, and the total internal energy in the fireball is provided by the shock heated ISM. Noticing equation (5), one can usually approximate  $U \simeq (\Gamma - 1)M_2c^2$  as a working assumption to perform a first-order treatment of the problem. Strictly speaking, such an approximation is only valid when the post-shock fluids are considered uniform, i.e., with constant density, temperature, and Lorentz factor. More detailed self-consistent modelings require taking into account the Blandford-McKee (1976) self-similar profiles and tracking the post-shock internal energy more closely. With the assumption, the integrated energy conservation equation then reads

$$E_{\text{inj}} + (\Gamma_0 - \Gamma)M_0c^2 = (\Gamma^2 - 1)M_2c^2. \quad (1)$$

This is analogous to the combination of equations (1) and (2) in Zhang & Mészáros (2001a). When  $E_{\text{inj}}$  is negligible and noticing that  $E_{\text{imp}} \simeq \Gamma_0M_0c^2$ , equation (1) is the standard equation for the impulsive adiabatic blastwave evolution (e.g. Chiang & Dermer 1999; Huang, Dai & Lu 1999), which can be reduced to the familiar form  $E_{\text{imp}} = (4\pi/3)R^3nm_pc^2\Gamma^2$  (so that  $\Gamma \propto R^{-3/2} \propto T^{-3/8}$ , where  $R$  is the blastwave radius in the fixed frame, and  $T$  is the observer time) when  $\Gamma_0 \gg \Gamma \gg 1$ . In the presence of  $E_{\text{inj}}$ , we can see that the condition for changing the blastwave dynamics is that  $E_{\text{inj}}$  exceed  $(\Gamma_0 - \Gamma)M_0c^2$ , or essentially  $E_{\text{inj}} \gtrsim E_{\text{imp}}$ .

A Poynting-flux-dominated wind is usually continuous, with an intrinsic luminosity law which may be defined through a temporal index  $q$  within a certain time regime, e.g.  $L(T) \propto T^q$ , where  $T$  is the intrinsic time of the central engine (which is the same as the observer's time after the cosmological time dilation correction). A detailed description of such an injection scenario, especially in the context of magnetar central engine models, was discussed in a previous paper (Zhang & Mészáros 2001a). Here we summarize some of the conclusions. When the blastwave dynamics is dominated by the injection (i.e.  $E_{\text{inj}} \gtrsim E_{\text{imp}}$ , which only occurs when  $q > -1$ ), the bulk Lorentz factor evolves according to  $\Gamma \propto R^{-(2-q)/2(2+q)} \propto T^{-(2-q)/8}$ . In most problems, usually  $q = 0$  during the injection phase, so that  $\Gamma \propto R^{-1/2} \propto T^{-1/4}$ . There are three relevant time scales in the problem, i.e., the blastwave deceleration time,  $T_0$ ; the critical time when the continuous-injection energy component dominates the impulsive-injection energy component,  $T_c$ ; and the characteristic time during which the central engine produces a substantial energy input (i.e.  $q > -1$ ),  $\mathcal{T}$ . The condition for the injection signature to show up in the afterglow lightcurves is  $\mathcal{T} > \max(T_c, T_0)$ . For  $T_c < T_0 < \mathcal{T}$ , the dynamics is defined by the continuous-injection as soon as the afterglow is set up, and we define it as an immediate injection (Fig.1a). The lightcurves will be flat from  $T_0$  to  $\mathcal{T}$ , and will steepen after  $\mathcal{T}$ . For  $T_0 < T_c < \mathcal{T}$ , the signature will not show up until  $T_c$ , and we define it as a delayed injection (Fig.1b). There are two temporal index changes: the lightcurves will flatten around  $T_c$ , and resume the original steepness around  $\mathcal{T}$ . The injection-signature is achromatic due to the change of the blast-

<sup>1</sup>The subscript 2 is used to match the notation in the kinetic-energy-dominated case discussed in §3, e.g., Figure 2 and equation (12).

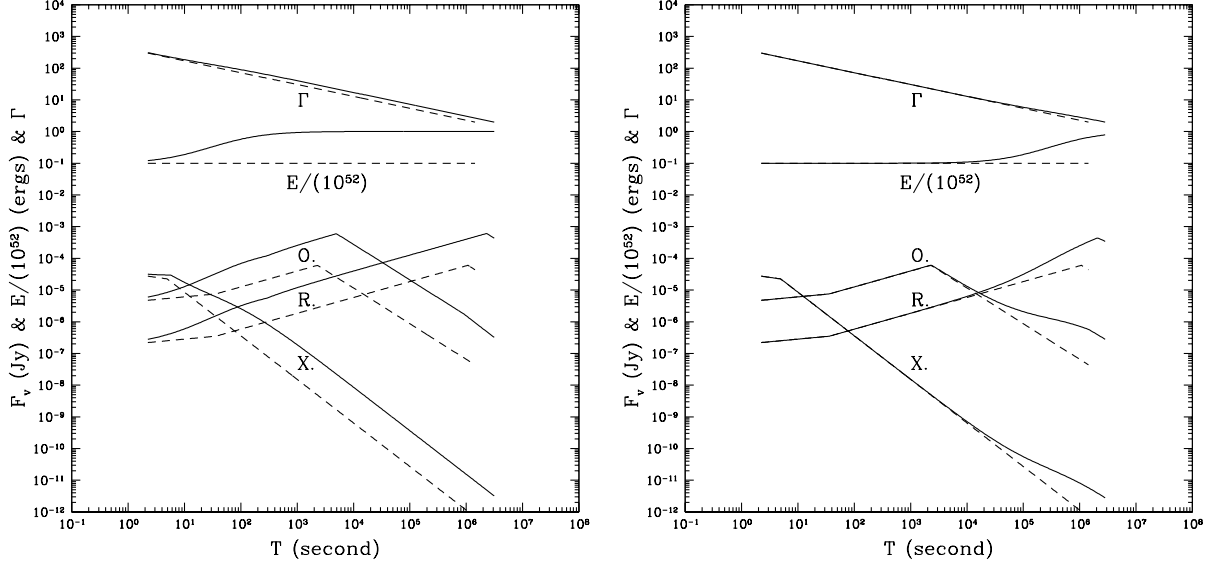


FIG. 1.— Injection lightcurves from a Poynting-flux-dominated flow ejected by a highly magnetized millisecond pulsar (magnetar) central engine. Solid and dashed lines are the cases with or without a continuous energy injection. Shown are the bulk Lorentz factor of the blastwave, the total energy in the fireball, as well as the lightcurves in various bands (X-ray:  $\nu = 10^{18}$  Hz; optical:  $\nu = 10^{14}$  Hz; radio:  $\nu = 10^{10}$  Hz). Parameters adopted:  $E_{\text{imp}} = 10^{51}$  ergs,  $n = 1 \text{ cm}^{-3}$ ,  $\Gamma_0 = 300$ ,  $\epsilon_e = 0.1$ ,  $\epsilon_B = 0.01$ , and  $p = 2.5$ . Different pulsar parameters lead to the injection being either “immediate” or “delayed”. (a) Immediate injection:  $B_p = 10^{16}$  G and  $P_0 = 1.5$  ms; (b) delayed injection:  $B_p = 10^{14}$  G and  $P_0 = 1.5$  ms.

wave dynamics. Since no reverse shock is expected, only emission from the forward shock is responsible for the afterglow emission. Assuming synchrotron emission of the relativistic electrons, the temporal index at the injection phase is  $\alpha = (1 - q/2)\beta + q + 1$  (which is  $\beta + 1$  for  $q = 0$ ), as compared to the standard case of  $\alpha = (3/2)\beta$ , where  $\beta$  is the spectral index in a certain band of interest. As an example, we again discuss the Poynting-flux injection case in the magnetar model. In this particular case, the injection luminosity law is  $L(T) = L_{\text{em},0}(1 + T/\mathcal{T}_{\text{em}})^{-2}$ , where  $L_{\text{em},0} = I\Omega_0^2/2\mathcal{T}_{\text{em}} \simeq 1.0 \times 10^{49} \text{ erg s}^{-1} B_{p,15}^2 P_{0,-3}^{-4} R_6^6$  and  $\mathcal{T}_{\text{em}} = 3c^3 I/B_p^2 R^6 \Omega_0^2 = 2.05 \times 10^3 \text{ s } I_{45} B_{p,15}^{-2} P_{0,-3}^2 R_6^{-6}$ , and  $B_p = 10^{15} \text{ cm} B_{p,15}$ ,  $P_0 = 10^{-3} \text{ s } P_{0,-3}$  are the pulsar dipolar field strength at the pole, and the initial period at birth,  $I = 10^{45} \text{ g cm}^2 I_{45}$  and  $R = 10^6 \text{ cm} R_6$  are the rotation inertia and the radius of the pulsar, respectively. Figure 1 shows two example injection lightcurves for both the immediate and the delayed injection cases in three energy bands. A general feature is that the injection signature is rather smooth, mainly due to the smooth varying luminosity law  $L(T)$ . Dai & Lu (2001) and Wang & Dai (2001) obtained a similar result recently.

### 3. INJECTION FROM A KINETIC-ENERGY-DOMINATED SHELL

The previous Poynting-dominated injection is, for the present purpose, the simplest case, in the sense that the injection does not result in new emission sites. The signature in the lightcurves is still produced by the shocked ISM, albeit through a changed global dynamics of the blastwave. However, if the injection energy is dominated by the kinetic energy of the baryons, collisionless shocks may in principle form at the discontinuity of any two adjacent

shells under certain conditions. The emission sites during the injection process therefore could be multiple, and the injection signatures, due to the joint contributions from all these sites, should be much more complicated. In this section, we investigate in some detail the shell collision process, as well as the emission signatures.

#### 3.1. Hydrodynamics

We consider a collision in the afterglow phase, in which case the impulsive shell is already heated up by the passage of the reverse shock. Assuming that the electron equipartition factor  $\epsilon_e$  is not close to unity, the impulsive shell will not cool at the time of injection, even if the electrons cool rapidly. A generic configuration of the problem is summarized in Figure 2, which is predicated upon the fulfillment of certain conditions (§3.2). There are six regions of interest, namely: (1) unshocked ISM; (2) forward-shocked ISM; (3) unshocked hot impulsive (leading) shell; (4) forward-shocked impulsive shell; (5) reverse-shocked injective (trailing) shell; (6) unshocked injective shell. We denote through  $M_i$ ,  $n_i$ ,  $e_i$  and  $p_i$  the mass, baryon number density, internal energy density, and the pressure of the region “ $i$ ” in its own rest frame, respectively;  $\gamma_i$  and  $\beta_i$  are the bulk Lorentz factor and the dimensionless velocity of region “ $i$ ” measured in the fixed frame, respectively; and

$$\gamma_{ij} \simeq (\gamma_i/\gamma_j + \gamma_j/\gamma_i)/2, \text{ for } \gamma_{i,j} \gg 1 \quad (2)$$

and  $\beta_{ij}$  the bulk Lorentz factor and the dimensionless velocity of region “ $i$ ” measured in the rest frame of region “ $j$ ”, respectively. In the hot regions (2, 3, 4 and 5), we assume a relativistic equation-of-state, i.e.,  $p_i = (\hat{\gamma} - 1)e_i = e_i/3$ , where  $\hat{\gamma} = 4/3$ . Two contact discontinuities separate the three parts, i.e., the ISM, the impulsive shell (which we

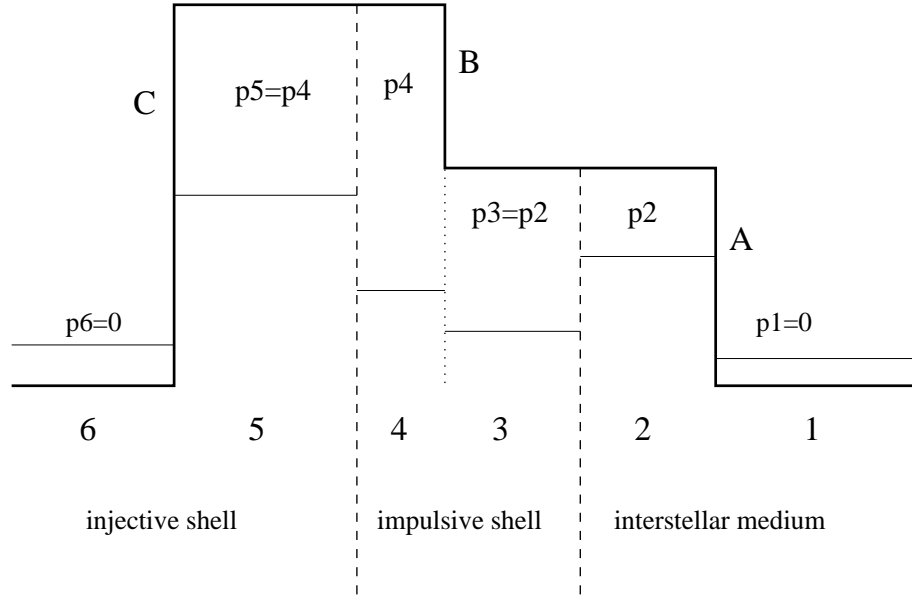


FIG. 2.— A schematic (not to scale) description of the violent injection configuration from a kinetic-energy-dominated shell. The thick solid line indicates the pressure, or the internal energy density, in each region. The thin solid line indicates the co-moving mass density in each region.

will consistently call shell 3 in the following discussions), and the injective shell (which we call shell 6 in the following discussions). The pressure equilibrium and velocity continuity at the contact discontinuities yield

$$e_3 = e_2, \quad \gamma_3 = \gamma_2, \quad (3)$$

$$e_5 = e_4, \quad \gamma_5 = \gamma_4. \quad (4)$$

There are three shocks that accelerate particles and contribute to the emission, i.e., (A) a first forward shock propagating into the ISM, (B) a second forward shock propagating into the impulsive shell, and (C) a reverse shock propagating into the injective shell. The continuity of the energy, momentum, and particle flux densities in the rest frame of each shock leads to the following jump conditions (Blandford & McKee 1976; Sari & Piran 1995; Kumar & Piran 2000)

$$\frac{e_2}{n_2} = (\gamma_2 - 1)m_p c^2, \quad \frac{n_2}{n_1} = 4\gamma_2 + 3, \quad (5)$$

$$\gamma_{43}^2 = \frac{(1 + 3e_4/e_3)(3 + e_4/e_3)}{16e_4/e_3}, \quad (6)$$

$$\left(\frac{n_4}{n_3}\right)^2 = \frac{(e_4/e_3)(1 + 3e_4/e_3)}{3 + e_4/e_3}, \quad (7)$$

$$\frac{e_5}{n_5} = (\gamma_{56} - 1)m_p c^2, \quad \frac{n_5}{n_6} = 4\gamma_{56} + 3. \quad (8)$$

Notice that the jump conditions at the second forward shock (eqs. [6] and [7]) are different from the others, mainly because the region in front of the shock (region 3) is hot. With (3) and (4), a combination of (5) and (8) yields

$$\frac{e_4}{e_3} = \frac{n_6}{n_1} \frac{F(\gamma_{56})}{F(\gamma_3)} \simeq \frac{E_{0,6}}{E_{0,3}} \cdot \frac{F(\gamma_{56})}{4} \cdot \min\left(1, \frac{R}{R_{s,6}}\right), \quad (9)$$

where

$$F(\gamma) = (\gamma - 1)(4\gamma + 3) \simeq 4\gamma^2, \quad \gamma \gg 1. \quad (10)$$

The second half of the equation (9) will be explained further below. Given  $\gamma_3$  and  $\gamma_6$ , the unknown  $\gamma_4$  can be solved for by replacing (9) into (6) with the use of (2).

### 3.2. Shell evolution & condition for violent collision

Equations (5)-(8) imply that strong shocks form between the contact discontinuity of the injective shell and the impulsive shell (e.g. Blandford & McKee 1976), as indicated in Figure 2. A physical solution for the non-linear equations (5)-(8) requires  $e_4 > e_3$ , or  $\gamma_3 < \gamma_4 < \gamma_6$ , which demands a minimum relative Lorentz factor between the two colliding shells given the parameters of both shells (eq.[9]). This is qualitatively in agreement with Kumar & Piran (2000), who demand a minimum enthalpy density ratio for a given  $\gamma_{36}$  (in their Fig.3), which is equivalent to our case in which we demand a minimum  $\gamma_{36}$  for a given  $E_{0,6}/E_{0,3}$ . For a shock to form, the injective shell should move super-sonically with respect to the impulsive shell, i.e., by noticing the sound speed  $c_s \simeq c/\sqrt{3}$  for the shell 3 (in the relativistic limit  $\hat{\gamma} = 4/3$ ),  $\gamma_{36} \geq \sqrt{3/2} \simeq 1.22$ . Usually this condition is automatically satisfied given the strong shock forming condition  $e_4 > e_3$ . In this subsection, we examine the criterion for  $e_4 > e_3$ , which is the condition for the configuration in Figure 2 being realized. We first summarize the evolution of a matter fireball shell (e.g. Mészáros, Laguna & Rees 1993; Piran, Shemi & Narayan 1993; Kobayashi, Piran & Sari 1999; Piran 1999), and then show how a shell collision process is well-defined by the initial conditions of the shells.

The injection of a matter shell from the central engine can be quantified by three independent parameters, i.e., the energy of the shell  $E_0$ , the mass of the shell

TABLE 1

Shell evolution: Evolution of the thickness ( $\Delta$  in the fixed frame,  $\Delta'$  in the comoving frame) and the comoving density  $n$  of a shell as a function of the fireball radius  $R$ .  $n_0 = M_0/[m_p(4\pi/3)\Delta_0^3]$  is the initial baryon number density.  $n_1$  is the density of the unshocked ISM, and  $M_2$  is the mass of the shocked ISM.

condition	radius regime	$\Delta'$	$\Delta$	$n$	$n/n_1$
	$\Delta_0 < R < R_c$	$R$	$\Delta_0$	$\frac{M_0}{\frac{4}{3}\pi R^3 m_p} = n_0 \left(\frac{\Delta_0}{R}\right)^3$	$M_0/M_2$
$R_s < R_d$	$R_c < R < R_s$	$R_c$	$\Delta_0$	$\left(\frac{M_0}{\frac{4}{3}\pi R^3 m_p}\right) \left(\frac{R}{R_c}\right) = n_0 \left(\frac{\Delta_0}{R}\right)^3 \left(\frac{R}{R_c}\right)$	$(M_0/M_2)(R/R_c) = (E_0/M_2 c^2)(R/R_s)$
(thin shell)	$R_s < R < R_d$	$R/\Gamma_0$	$R/\Gamma_0^2$	$\left(\frac{M_0}{\frac{4}{3}\pi R^3 m_p}\right) \Gamma_0 = n_0 \left(\frac{\Delta_0}{R}\right)^3 \Gamma_0$	$(M_0/M_2)\Gamma_0 = E_0/M_2 c^2$
	$R > R_d$	$R/\Gamma$	$R/\Gamma^2$	$\left(\frac{M_0}{\frac{4}{3}\pi R^3 m_p}\right) \Gamma = n_0 \left(\frac{\Delta_0}{R}\right)^3 \Gamma$	$(M_0/M_2)\Gamma = (E_0/M_2 c^2)(\Gamma_0/\Gamma)$
$R_s > R_d$	$R_c < R < R_d$	$R_c$	$\Delta_0$	$\left(\frac{M_0}{\frac{4}{3}\pi R^3 m_p}\right) \left(\frac{R}{R_c}\right) = n_0 \left(\frac{\Delta_0}{R}\right)^3 \left(\frac{R}{R_c}\right)$	$(M_0/M_2)(R/R_c) = (E_0/M_2 c^2)(R/R_s)$
(thick shell)	$R > R_d$	$R/\Gamma$	$R/\Gamma^2$	$\left(\frac{M_0}{\frac{4}{3}\pi R^3 m_p}\right) \Gamma = n_0 \left(\frac{\Delta_0}{R}\right)^3 \Gamma$	$(M_0/M_2)\Gamma = (E_0/M_2 c^2)(\Gamma_0/\Gamma)$

$M_0$  (thus the dimensionless entropy, or the maximum Lorentz factor of the shell is  $\eta = \Gamma_0 = E_0/M_0 c^2$ ), and the initial thickness of the shell  $\Delta_0$  which is essentially determined by the timescale of the central engine activity, i.e.,  $\Delta_0 = c\delta T$ . The following parameters can be consequently defined: the initial baryon number density of the shell, which is  $n_0 = M_0/[m_p(4\pi/3)\Delta_0^3]$ ; the radius at which the fireball stops accelerating and enters the coasting phase, which is  $R_c \simeq \Gamma_0 \Delta_0$ ; and the radius at which the fireball starts to spread with its local sound speed due to the velocity difference within the fireball matters, which is  $R_s \simeq \Gamma_0^2 \Delta_0$ . There is another parameter, i.e., the deceleration radius  $R_d$ , which usually appears in the problem. However, this radius not only depends on the intrinsic parameters of the shell (e.g. total energy), but also on the properties (e.g. density and velocity) of the medium that stops the shell. For the interaction between the impulsive shell (shell 3) and the ISM, the deceleration radius is roughly the radius where the mass of the ISM collected by the fireball is  $1/\gamma_{0,3}$  of the shell mass, i.e.,  $R_{d,3} \sim R_{\gamma,3} = (3E_{0,3}/4\pi n_1 m_p c^2 \eta_3^2)^{1/3} = 1.2 \times 10^{16} \text{ cm } E_{0,3,51}^{1/3} n_1^{-1/3} (\gamma_{0,3}/300)^{-2/3}$ , where  $n_1$  is the ISM baryon number density in unit of  $1 \text{ cm}^{-3}$ ,  $E_{0,3,51} = E_{0,3}/10^{51} \text{ ergs}$  (hereafter  $X_n = X/10^n$ , except those subscripts that denote different regions, such as  $n_1$ ). For the interaction between the injective shell (shell 6) and the impulsive shell (shell 3), the deceleration radius is around the radius where the injective shell catches up with the impulsive shell. Let us denote  $\Delta T_{36}$  as the time interval between ejecting the two adjacent shells (as compared to  $\delta T$ , which is the timescale of the injection process), the “catching-up” radius is then  $R_{d,6} \simeq 2\gamma_3^2 c(\Delta T_{36})/(1 - \gamma_3^2/\gamma_6^2)$ . For  $\gamma_6 \gg \gamma_3$ ,  $R_{d,6}$  is mainly defined by the Lorentz factor of the slow, leading shell, i.e.,  $R_{d,6} \simeq 2\gamma_3^2 c(\Delta T_{36}) = 2.1 \times 10^{16} \text{ cm } E_{0,3,51}^{1/4} (\Delta T_{36}/20 \text{ s})^{1/4} n_1^{-1/4}$ . The condition for the collision to occur in the afterglow phase is then  $R_{d,6} > R_{d,3}$ , or approximately  $\Delta T_{36} > 2.3 \text{ s } E_{0,3,51}^{1/3} n_1^{-1/3} (\gamma_{0,3}/300)^{-8/3}$ . The deceleration radius of a shell can in principle be either smaller or larger than the spreading radius,  $R_s$ . For  $R_s > R_d$  (a “thick shell”, e.g. Sari & Piran 1995), the shell has not started to spread when the deceleration (or the collision) occurs. Alternatively, for a “thin shell” (with  $R_s < R_d$ ), the shell is spreading with its sound speed in the comoving frame due

to the velocity difference within the shell as the collision occurs. In this sense, the initial “thin shell” is actually thick during the collision. Table 1 summarizes the evolution of the shell widths (both in the fixed frame,  $\Delta$ , and in the comoving frame,  $\Delta'$ ), shell baryon number density  $n$ , and the ratio  $n/n_1$  in various regimes. In the last column (i.e.,  $n/n_1$ ), for the rear shell 6, we have assumed that the radius of the shell 6 front is comparable to that of the shell 3 front, i.e., we assume that  $\Delta_3 \ll R$ , which is generally the case as long as  $\gamma_3 \gg 1$ . We note that expressing  $n/n_1$  in terms of the mass (or energy) ratio of the shell and the collected ISM ( $M_2$ ) allows a clearer physical understanding for the problem. At the collision point  $R_{d,6}$ , it is convenient to show that  $n_6/n_1 = (M_{0,6}/M_2) \cdot \min(R/R_{c,6}, \gamma_{0,6})$  (thick shells for the former, and thin shells for the latter). Noticing that  $\gamma_6 M_{6,0} = E_{\text{inj}} = E_{0,6}$ , and that for  $\gamma_{0,3} \gg \gamma_3 \gg 1$  (i.e., the collision occurs long after the afterglow’s setting-up but well before the non-relativistic phase, which is usually the case), one has  $F(\gamma_3) \simeq 4\gamma_3^2$ , and  $\gamma_3^2 M_2 \simeq E_{\text{imp}} = E_{0,3}$  (see eq.[12] and the discussions thereafter). This justifies the second part of the equation (9).

The condition for  $e_4 > e_3$  can be investigated numerically. Figure 3 shows the minimum  $\gamma_{36}$  required for  $e_4 > e_3$  for different energy ratios of the two shells,  $E_{0,6}/E_{0,3}$ . Notice that the wiggles on the curves are due to the crudeness of the numerical solutions. A general trend is that a larger relative velocity between the two shells is required for a less energetic trailing shell. The critical line depends on the status of the shell 6, i.e., whether it is expanding (thin shell) or not (thick shell) when the collision occurs. This is least demanding for an expanding (thin) shell 6, which is plotted as the solid curve. For a thick shell 6, the larger the ratio  $R_s/R$ , the more demanding the condition is. This is because for the same energy ratio  $E_{0,6}/E_{0,3}$ , a thicker shell tends to get a smaller  $e_4/e_3$  ratio (eq.[9]). The dotted and the dashed curves in Figure 3 are for a shell with  $R_{s,6}$  5 and 10 times the collision radius,  $R_{d,6}$ , respectively. Another comment is that, as long as in the relativistic phase lasts, only the energy ratio and the relative velocity are relevant to the problem. The absolute values of the shell energies and Lorentz factors do not enter the solution. Notice that the supersonic condition defines another critical line for the shock forming condition (Fig.3). The case for  $e_4 > e_3$  not being satisfied is less clear, but in this case no strong shock is expected. We regard such an

injection case as “mild” (with weak or non-shock), and we expect that the injective materials are effectively attached onto the forward shell to increase the total energy budget, which is analogous to the Poynting-flux injection case.

In summary, the input parameters in the injection problem include: (i)  $E_{\text{imp}} = E_{0,3} = \gamma_{0,3} M_{0,3} c^2$ ; (ii)  $\gamma_{0,3}$  (or  $M_{0,3}$ , which is only important around the on-set of the afterglow); (iii)  $n_1$ ; (iv)  $E_{\text{inj}} = E_{0,6} = \gamma_{0,6} M_{0,6} c^2$ ; (v)  $\gamma_{0,6}$  (or  $M_{0,6}$ ); (vi)  $\Delta_{0,6} = c\delta T_6$ , which determines  $R_{s,6} = \gamma_{0,6}^2 \Delta_{0,6}$ ; (vii)  $\Delta T_{36}$  (or equivalently  $R_{d,6}$ ). The comparison between  $R_{s,6}$  and  $R_{d,6}$  then decides whether the trailing shell is “thin” or “thick” when the collision occurs. Given a set of injection parameters (i) - (vii), at any radius  $R$ , one can first check the shock forming condition in Figure 3. If the condition is not satisfied (below the critical line), the injection is a “mild” one. If the condition is satisfied (above the critical line in Fig.3), the shell-merging process is violent.

### 3.3. Shell merging process

Though an injection of matter shell could be mild or violent throughout, in some cases the injection could be mild in the beginning, and turn violent at larger radii when  $\gamma_3$  drops so that  $\gamma_{36}$  meets the critical value. In this subsection, we present an example which includes both cases during the injection. There are four characteristic radii in the problem: (1) the collision radius,  $R_{\text{col}} = R_{d,6}$ ; (2) the radius where the persistent shocks form (Fig.3),  $R_{sh}$ ; (3) the radius where the injection process ceases,  $R_{\Delta}$ ; (For a mild injection, this is the radius where all the material in the shell 6 catches up with and “attaches” onto shell 3; for a violent injection, this is where the reverse shock crosses the rear shell and the merging process enters the relaxation stage.) (4) the radius where  $e_4/e_3$  drops to unity and the relaxation finishes,  $R_f$ . The whole shell-merging process may be then be (at most) divided into five stages (Fig.4a): (1) pre-collision,  $R < R_{\text{col}}$ ; (2) mild injection,  $R_{\text{col}} < R < R_{sh}$ ; (3) violent injection,  $R_{sh} < R < R_{\Delta}$ ; (4) relaxation,  $R_{\Delta} < R < R_f$ ; and (5) post-relaxation,  $R > R_f$ . Below we discuss each stage in some detail.

#### 3.3.1. Pre-collision stage

Let us consider a central engine that ejects an impulsive fireball<sup>2</sup> (shell 3) with  $E_{\text{imp}} = E_{0,3} = \gamma_{0,3} M_{0,3} c^2$ . Some time ( $\Delta T_{36}$ ) later, it ejects another (effective) shell (shell 6) with  $E_{\text{inj}} = E_{0,6} = \gamma_{0,6} M_{0,6} c^2$ . The forward shell starts to decelerate at  $R_{d,3}$  due to the interaction with the ISM, and at a certain time before collision, it has collected a mass  $M_2$  worth of ISM, and has a Lorentz factor of  $\gamma_3$ . The rear shell moves faster, and we assume that before collision it is essentially undecelerated, and is still propagating with  $\gamma_{0,6}$ . The whole system has two independent sub-systems. The deceleration of the forward shell is quantified by (cf. eq.[1] but without the injection term)

$$(\gamma_{0,3} - \gamma_3) M_{0,3} = (\gamma_3^2 - 1) M_2 , \quad (11)$$

which is the standard adiabatic afterglow evolution. The rear shell is not noticeable at this stage.

#### 3.3.2. Mild injection stage

Starting from  $R_{\text{col}} = R_{d,6} \simeq 2\gamma_3^2(c\Delta T_{36})$ , the shell 6 catches up with the shell 3. At  $R_{\text{col}} < R < R_{sh}$ , the injection is not energetic enough to excite shocks. The injection is analogous to the case of a Poynting-flux-dominated flow, i.e., mainly it increases the blastwave energetics. Assuming that at a certain radius (time) a mass of  $M_5$  from the total injection shell  $M_{6,0}$  reaches the shell 3 and its energy is added to the total blastwave energy (here the subscript 5 is only for easy comparison with the following notations, eqs.[13], [14] and [18], but does not have the physical meaning illustrated in Fig.2), one can write down the global energy conservation of the system. The total energy of the two shells and the (collected) ISM if there were no interaction among them is  $(\gamma_{0,6} M_{0,6} + \gamma_{0,3} M_{0,3} + M_2) c^2$ ; that with the interactions is  $\gamma_{0,6} (M_{0,6} - M_5) c^2 + \gamma_3 (M_5 c^2 + M_{0,3} c^2 + U_{2+3+5})$ . These two should be equal. Noticing that  $U_{2+3+5} \simeq (\gamma_3 - 1) M_2 c^2$ , one has

$$(\gamma_{0,6} - \gamma_3) M_5 + M_{0,3} (\gamma_{0,3} - \gamma_3) = (\gamma_3^2 - 1) M_2 . \quad (12)$$

This is very analogous to (1). For  $\gamma_{6,0} \gg \gamma_3$ , the first term on l.h.s is approximately  $\gamma_{6,0} M_5$ , which is just the energy injected into the system.

During this mild injection phase, the mass in the shell 3 gradually increases while that in the shell 6 (un-collided part) gradually decreases. This ends when the  $e_4 > e_3$  condition is satisfied at  $R_{sh}$  and a pair of shocks (B and C) propagate into the two colliding shells, or, in a less energetic situation, when the whole shell 6 is “attached” onto the shell 3 and the injection process ceases. For the former case, we define  $E_{sh,3} = E_{0,3} + M_5 c^2$  and  $E_{sh,6} = E_{0,6} - M_5 c^2$ , both of which will be used later in the stage 4 (§3.3.4).

#### 3.3.3. Violent injection stage

If the shell 6 is energetic enough or fast enough (see Fig.3), one then has the configuration shown in Figure 2. The two new shocks (B and C) propagate into the two colliding shells, respectively. In principle, one can define this stage to end when either of the two shocks crosses the corresponding shell. However, the reverse shock always crosses the rear shell first, and we define the radius where this happens as  $R_{\Delta}$ . The violent injection stage is then defined as  $R_{sh} < R < R_{\Delta}$ .

To describe the physical process at this stage, we need to quantify the dynamical evolution of the three shocks, or equivalently, the temporal evolution of  $\gamma_3 = \gamma_2$  and  $\gamma_5 = \gamma_4$ . Strictly speaking,  $\gamma_3$  and  $\gamma_4$  should be solved self-consistently, and one needs one more independent relation between  $\gamma_3$  and  $\gamma_4$  besides (6) and (9), in order to get a self-consistent solution. However, this is usually not necessary at this stage. Again, we write down the global energy conservation of the whole system, i.e.,  $\gamma_{0,6} M_{0,6} c^2 + \gamma_{0,3} M_{0,3} c^2 + M_2 c^2 = \gamma_{0,6} (M_{0,6} - M_5) c^2 + \gamma_4 (M_5 c^2 + M_4 c^2 + U_{4+5}) + \gamma_3 (M_2 c^2 + M_{0,3} c^2 - M_4 c^2 + U_{2+3})$ . Noticing  $U_{2+3} \simeq (\gamma_3 - 1) M_2 c^2$ ,  $U_{4+5} \simeq (\gamma_{56} - 1) M_5 c^2$ , this gives a time-dependent equation

$$(\gamma_{0,6} - \gamma_4 \gamma_{56}) M_5 - (\gamma_4 - \gamma_3) M_4 + (\gamma_{0,3} - \gamma_3) M_{0,3} = (\gamma_3^2 - 1) M_2 . \quad (13)$$

<sup>2</sup>The impulsive fireball could be in principle highly erratic, as indicated by spiky GRB lightcurves. In the afterglow phase, many mini-shells collide and merge into one big shell, and we regard this as equivalent to the central engine effectively ejecting one single shell.

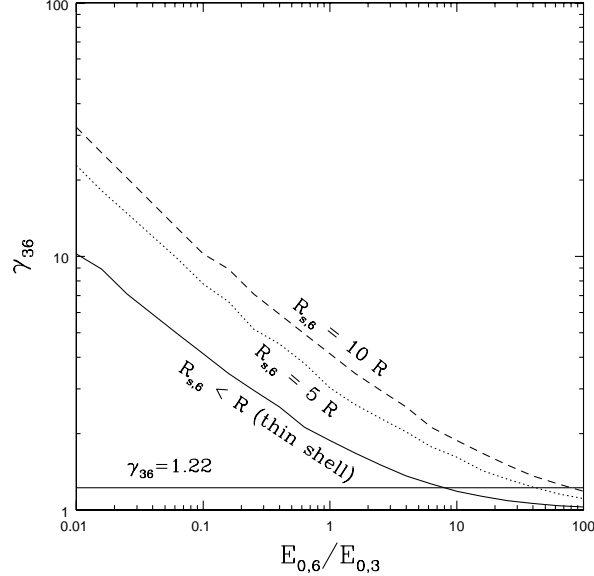


FIG. 3.— The condition for a violent injection. The three curves are the critical lines for  $e_4 > e_3$  being satisfied, for different cases of the rear shell (thin or thick at the collision). The super-sonic condition (the horizontal line) is also plotted. The space region above both the critical line and the horizontal line is where a violent collision as indicated in Fig.2 occurs.

Comparing to equations (12) and (1), we find that the first term in those equations (the already injected energy) is now replaced by the first two terms in (13). The global dynamics ( $\gamma_3$  evolution) is modified only when the sum of the first two terms is comparable to the third term which is essentially  $E_{\text{imp}}/c^2 = \gamma_{0,3}M_{0,3}$ . This is impossible, since the energy already injected into the system (i.e.  $\gamma_{0,6}M_5$ ) is now partially consumed in maintaining the kinetic energy of the injected material [i.e.,  $-\gamma_4\gamma_{56}M_5c^2$ , since for  $\gamma_{0,6} \gtrsim \gamma_3$  the term  $(\gamma_{0,6} - \gamma_4\gamma_{56})$  is nearly zero], and in raising the Lorentz factor of the newly shocked regions [i.e. the term  $-(\gamma_4 - \gamma_3)M_4$ ]. Unless  $E_{\text{inj}} \gg E_{\text{imp}}$ , which is rather unlikely in GRBs, the sum of the first two terms is negligibly small, and (13) is essentially reduced to (11). The simple scaling law of  $\gamma_3$  for the impulsive injection case is then applicable at this stage, e.g., for an isotropic adiabatic fireball running into a uniform ISM, one has  $\gamma_3 \propto R^{-3/2} \propto T^{-8/3}$ .

The unknown quantity  $\gamma_4$ , of interest here, can then be solved for by using (6) and (9). The temporal evolution of both  $\gamma_{34}$  and  $\gamma_{56}$ , as well as the random Lorentz factor in the region 4,  $\gamma_B$ , are thus well quantified. Although generally this is done numerically, a rough analytic estimate is possible. When the solution of  $\gamma_4$  is physical, one can approximate  $\gamma_6 \gg \gamma_4 \gg \gamma_3$ , as long as  $\gamma_6/\gamma_3 \gg 1$ . In this limit,  $\gamma_{56} \sim \gamma_6/2\gamma_4$ ,  $\gamma_{43} \sim \gamma_4/2\gamma_3$ , and one has  $\gamma_4 \propto (n_6/n_1)^{1/4}\gamma_6^{1/2}$ . For our assumption of  $\gamma_6 \sim \gamma_{6,0} = \text{const}$ , we have  $\gamma_4 \propto n_6^{1/4} \propto R^{-3/4}$  for a spreading shell ( $\propto R^{-1/2}$  for a non-spreading shell<sup>3</sup>). We can further estimate  $e_4/e_3 \propto \gamma_{43}^2 \propto n_6^{1/2}R^3 \propto R^{3/2}$  (or  $\propto R^2$ ). Since  $e_3 \propto \gamma_3^2 \propto R^{-3}$ , we have  $e_4 \propto n_6^{1/2} \propto R^{-3/2}$  (or  $\propto R^{-1}$ ). With (7), we also have  $n_4/n_3 \propto (e_4/e_3)^{1/2} \propto$

$R^{3/4}$  (or  $\propto R$ ). Noticing that the shell 3 is spreading and that  $n_3 \propto R^{-3}\gamma_3 \propto R^{-9/2}$ , one then has  $n_4 \propto R^{-15/4}$  (or  $\propto R^{-7/2}$ ). The “random” Lorentz factor in the region 4 (at the shock B) which defines the radiation from the region (notice that it is different from  $\gamma_{43}$ ) is then  $\gamma_B = e_4/n_4 m_p c^2 \propto n_6^{1/4} R^3 \propto R^{9/4}$  (or  $\propto R^{5/2}$ ). Finally, the random Lorentz factor at the shock C is essentially  $\gamma_C = \gamma_{56}$ , which scales as  $\propto n_6^{-1/4} \propto R^{3/4}$  (or  $\propto R^{1/2}$ ). These very crude estimates generally agree with the numerical results (see Fig.4a).

Finally we estimate  $R_\Delta$ . A self-consistent calculation of the shock crossing time (for both shells) requires hydrodynamically tracking the speeds of the shocked and un-shocked shells. Very roughly, the shock crossing time (e.g., for the rear shell 6) may be estimated (Sari & Piran 1995)  $t_{\Delta_6} = [\bar{\Delta}_6/c(\beta_6 - \bar{\beta}_5)] \cdot (1 - \gamma_6 \bar{n}_6 / \bar{\gamma}_5 \bar{n}_5) \sim (\bar{\Delta}_6/c)\bar{\gamma}_4^2$  (for  $\gamma_6 \gg \gamma_5 = \gamma_4 \gg \gamma_3$ ), where  $\bar{x}$  denotes the average value of the quantity  $x$  during the passing process. This estimation is only good for a not very long passing time, so that the variables do not change much during the crossing period. This is the case for the rear shell, but not for the forward shell. For example, for a thin rear shell,  $\Delta \sim R/\gamma_6^2$ , and  $t_{\Delta_6} \sim (R/c)(\bar{\gamma}_4/\gamma_6)^2$ . This is much less than the dynamical time of the shell propagation in the fixed frame,  $R/c$ , as long as  $\gamma_4 \ll \gamma_6$ . For a thick rear shell, the crossing time is even shorter since the shell is not spreading. For the forward shell, however, one has  $t_{\Delta_3} \sim (R/c)$ , which is very long. Therefore it is evident that  $t_{\Delta_6}$  is always shorter than  $t_{\Delta_3}$ , and we use it to define the end of the collision stage. The radius  $R_\Delta$  is then defined as  $\sim R_{\text{col}} + ct_{\Delta_6}$ , and we denote the corresponding parameters at this radius with a subscript “ $\Delta$ ”, e.g.,  $e_{\Delta,3}$ ,  $e_{\Delta,4}$ ,  $\gamma_{\Delta,3}$ ,  $\gamma_{\Delta,4}$ , etc. These quantities are recorded from

<sup>3</sup>Hereafter the scaling for an spreading shell is not bracketed, while that for a non-spreading shell is.

the code and are inputs to the dynamical problem of the next stage (see below).

### 3.3.4. Relaxation stage

Beyond  $R_\Delta$ , the reverse shock passes across the rear shell, and the process enters the dynamical relaxation stage. After this point, there is no further significant energy input into the region (4+5). Since  $e_4 > e_3$  is still satisfied at  $R_\Delta$ , the forward shock B still exists and propagates into the forward shell as long as the region (4+5) is separated from the region (2+3) super-sonically. The region (4+5) then expands adiabatically, since there is practically no heat flow across the shock. The internal energy density in the region (4+5) decreases according to the adiabatic law, i.e.,  $e_4 \propto U_{4+5}/V' \propto (V')^{-\hat{\gamma}} \propto R^{-4}\gamma_4^{4/3}$  for  $\hat{\gamma} = 4/3$ . As a result,  $e_4/e_3$  as well as  $\gamma_{43}$  drops rapidly towards unity. During this process,  $\gamma_3$  increases and  $\gamma_4$  drops, until the whole region (2+3+4+5) reaches the same velocity, and contacts sub-sonically. The shock (B) disappears and the relaxation stage ends, at the radius defined by  $R_f$ .

During the relaxation stage, the shock conditions (5), (6) and (7) still hold. Again one needs to quantify the dynamical evolution of  $\gamma_3$  and  $\gamma_4$ . Unlike the previous stage,  $\gamma_3$  no longer evolves according to the simple  $\propto R^{-3/2}$  form. Let us again write down the global energy conservation of the whole system, i.e.,  $\gamma_{0,6}M_{0,6}c^2 + \gamma_{0,3}M_{0,3}c^2 + M_2c^2 = \gamma_4(M_{0,6}c^2 + M_4c^2 + U_{4+5}) + \gamma_3(M_{3,0}c^2 - M_4c^2 + M_2c^2 + U_{2+3})$ . Noticing that the shock heating energy produced at (A) is only consumed in the region (2+3), i.e.,  $U_{2+3} \simeq (\gamma_3 - 1)M_2c^2$ , this gives

$$(\gamma_{0,6} - \gamma_4)M_{0,6} - (\gamma_4 - \gamma_3)M_4 - \gamma_4U_{4+5} + (\gamma_{0,3} - \gamma_3)M_{0,3} = (\gamma_3^2 - 1)M_2. \quad (14)$$

This is even more complicated than (13). As the relaxation goes on,  $\gamma_4$  gets closer to  $\gamma_3$  and  $U_{4+5}$  drops rapidly, thus both the second and the third terms decline. The first term, which is essentially the injected energy, starts to influence the blastwave dynamics, just like the Poynting-flux injection or the mild injection (stage 2) cases (cf. eqs.[1] and [12]).

The relaxation is a complicated process. Strictly speaking, one needs to solve (14) and (6) to find a self-consistent solution for  $\gamma_3$  and  $\gamma_4$ . Here we perform a simpler but adequate treatment. Since  $\gamma_3$  is boosted up relative to the non-injection case, we assume that

$$\gamma_3^2 \propto e_3 \propto R^{-3+\delta}, \quad (15)$$

where  $\delta$  is an unknown positive index. At  $R_f$ , the internal energy density of the whole fireball is then  $e_{3,f} = e_{\Delta,3}(R_\Delta/R_f)^{3-\delta}$ . Since beyond  $R_f$  the fireball evolves as if the initial total energy is  $E_{0,6} + E_{0,3} = E_{sh,6} + E_{sh,3}$ , then  $e_{3,f}$  can be also expressed in an adiabatic expansion form, but as if the energy density at  $R_\Delta$  is a factor  $(1 + E_{sh,6}/E_{sh,3})$  times larger, i.e.,  $e_{3,f} = (1 + E_{sh,6}/E_{sh,3})e_{\Delta,3}(R_\Delta/R_f)^3$ . This gives

$$\delta = \frac{\ln \left( 1 + \frac{E_{sh,6}}{E_{sh,3}} \right)}{\ln \left( \frac{R_f}{R_\Delta} \right)}. \quad (16)$$

The last task is to determine  $R_f$ . In the relaxation stage,  $e_3$  can be expressed as  $= e_{\Delta,3}(R_\Delta/R)^{3-\delta}$ , according to the assumption made. On the other hand,  $e_4$  evolves according to the adiabatic law, i.e.,  $e_4 = e_{\Delta,4}(R_\Delta/R)^4(\gamma_4/\gamma_{\Delta,4})^{4/3}$ . One then has  $e_4/e_3 = (e_{\Delta,4}/e_{\Delta,3})(R_\Delta/R)^{(9+\delta)/3}(\gamma_{\Delta,3}/\gamma_{\Delta,4})^{4/3}(\gamma_4/\gamma_3)^{4/3}$ . At  $R = R_f$ ,  $e_4/e_3 = 1$  and  $\gamma_4/\gamma_3 = 1$  by definition. Noticing again equation (15), the relaxation stage ends at

$$R_f = R_\Delta \left( \frac{e_{\Delta,4}}{e_{\Delta,3}} \right)^{1/3} \left( \frac{\gamma_{\Delta,3}}{\gamma_{\Delta,4}} \right)^{4/9} \left( 1 + \frac{E_{sh,6}}{E_{sh,3}} \right)^{-1/9}. \quad (17)$$

Since the parameters at  $R_\Delta$  are in principle known (§3.3.3), equations (15)-(17), together with (5) and (6), adequately describe the dynamics in the relaxation stage.

Some crude estimates match the numerical results. With  $e_4 \propto R^{-4}\gamma_4^{4/3}$ ,  $e_3 \propto R^{-(3+\delta)}$  and  $\gamma_{43}^2 \propto e_4/e_3$  (eq.[6]), one can get, roughly,  $\gamma_4 \propto R^{-6}$ , a very steep declination (Fig.4a). As long as the shock (B) still exists, new electrons are accelerated, and strong emission from the region heated by the shock (B) continues throughout the relaxation stage. At the rear end of the shell (the region 5), since there is no longer a reverse shock (C), no new electrons are accelerated. However, the already accelerated electrons are still hot and radiate synchrotron emission. The random Lorentz factor in the region 5, which we still denote as  $\gamma_c$  (although the shock (C) no longer exist), also drops rapidly. Since  $e_5 = e_4 \propto (V')^{-\hat{\gamma}} \propto R^{-4}\gamma_4^{4/3}$ , and  $n_5 \propto (V')^{-1} \propto R^{-3}\gamma_4$ , one has  $\gamma_c \propto (V')^{-\hat{\gamma}+1} \propto R^{-1}\gamma_4^{1/3} \propto R^{-3}$  (Fig.4a). Since  $e_4/e_3$  no longer  $\gg 1$ , there is no simple scaling-law estimation of  $\gamma_b$  at this stage.

### 3.3.5. Post-relaxation stage

After the relaxation ends, one has  $\gamma_3 = \gamma_4$ , the original  $U_{4+5}$  has died out, and the new thermal energy produced at the shock (A) is consumed in the whole shell (2+3+4+5), i.e.,  $U_{2+3+4+5} \simeq (\gamma_3 - 1)M_2c^2$ . The global energy conservation now reads  $\gamma_{0,6}M_{0,6}c^2 + \gamma_{0,3}M_{0,3}c^2 + M_2c^2 = \gamma_3(M_{0,6}c^2 + M_{3,0}c^2 + U_{2+3+4+5})$ , which is

$$(\gamma_{0,6} - \gamma_3)M_{0,6} + (\gamma_{0,3} - \gamma_3)M_{0,3} = (\gamma_3^2 - 1)M_2. \quad (18)$$

This can be also obtained by removing the second and third terms in (14), as required by the physical relaxation process. Equation (18) is a standard adiabatic expansion equation with a total energy of  $\gamma_{0,6}M_{0,6}c^2 + \gamma_{0,3}M_{0,3}c^2 = E_{\text{inj}} + E_{\text{imp}}$ . At this stage, the only shock that accelerates new electrons is the shock (A), and the emission from it is well described by the standard afterglow theory.

Although shocks (B) and (C) no longer exist, their already accelerated electrons are still present and emitting. The random Lorentz factors in both regions (4 and 5), which we still denote as  $\gamma_b$  and  $\gamma_c$ , evolve as  $\propto (V')^{-\hat{\gamma}+1} \propto R^{-1}\gamma_3^{1/3} \propto R^{-3/2}$  (Fig.4a).

### 3.4. Synchrotron radiation and injection lightcurves

With the shell-merging dynamics quantified above, we can calculate the injection signatures in the afterglow lightcurves. We have developed a code to calculate the dynamics of the shell merging process as well as the emission

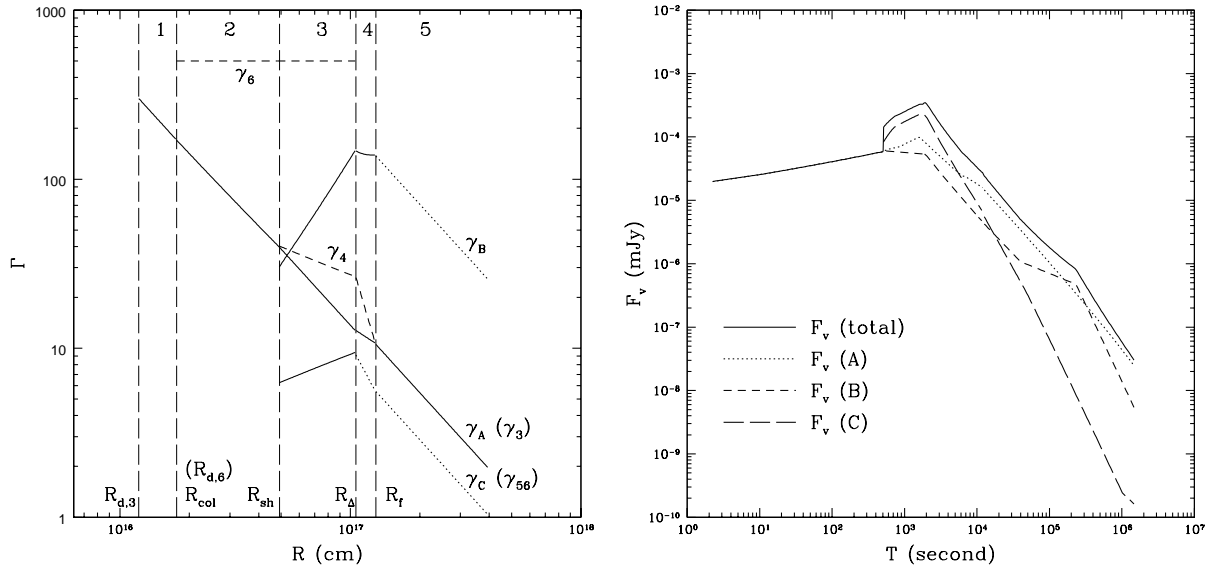


FIG. 4.— An example of the kinetic-energy-dominated shell injection case. Parameters: for the impulsive shell 3, total energy  $E_{0,3} = 10^{51}$  ergs, dimensionless entropy  $\gamma_{0,3} = 300$ ; for the injective shell 6,  $E_{0,6} = 5 \times 10^{50}$  ergs, and  $\gamma_{0,6} = 500$ . The central engine activity time for the rear shell is  $\delta T_6 = 100$  s, the time interval between ejecting the two shells is  $\Delta T_{36} = 10$  s. ISM baryon number density  $n_1 = 1 \text{ cm}^{-3}$ , electron spectral index  $p = 2.5$ . Equipartition parameters  $\epsilon_e = 0.1$ , and  $\epsilon_B = 0.02$ . The source redshift  $z = 1$ . (a) Evolution of various Lorentz factors with blastwave radius  $R$ .  $\gamma_A$ ,  $\gamma_B$ , and  $\gamma_C$  are the random Lorentz factors of the emission sites heated by the shocks (A), (B), and (C), respectively. The curves are solid when the shocks are on, and are dotted when they are off.  $\gamma_3$ ,  $\gamma_4$ , and  $\gamma_6$  are the bulk Lorentz factors of the regions (2+3), (4+5), and 6, respectively (cf. Fig.2). Four critical radii, i.e.,  $R_{col}$ ,  $R_{sh}$ ,  $R_\Delta$  and  $R_f$ , separate the process into 5 stages, as marked in the plot. (b) The injection lightcurve in the optical band ( $\nu = 10^{14}$  Hz). The emission components from all the three sites as well as the total flux are plotted.

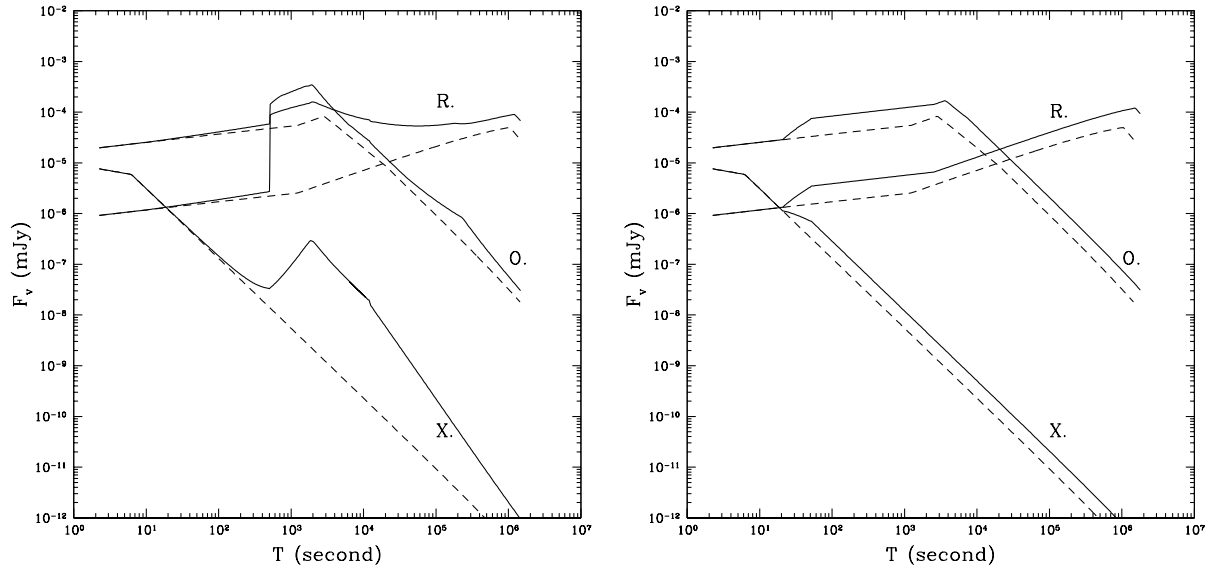


FIG. 5.— Broadband injection signatures (X-ray, optical, and radio) for the injection of a kinetic-energy-dominated shell. Solid lines are lightcurves with injection, compared to the dashed line case without injection. (a) A “violent” injection involving formation of new shocks. All the parameters are the same as adopted in Figure 4. (b) A mild injection. Injective shell parameters are  $E_{0,6} = 1 \times 10^{51}$  ergs,  $\gamma_{0,6} = 200$ . The central engine activity time for the rear shell is  $\delta T_6 = 20$  s, the time interval between ejecting the two shells is  $\Delta T_{36} = 20$  s. Other parameters are the same as in Fig.4 and Fig.5a. Notice that although the total energy for the shell 6 is higher in the present case, the relative Lorentz factor between the two shells is much smaller, and the injection is mild.

from various shocks. Since the normal afterglow emission is generally well described by synchrotron radiation, we have neglected the high energy spectral components, such as the electron inverse Compton and the emission from the protons. Although these components could be important in the MeV to GeV range (see Zhang & Mészáros 2001b for a detailed discussion), usually synchrotron emission is adequate to describe the low energy afterglow (X-ray, optical and radio), at least in the early afterglow phase when injection may be expected. Nonetheless, the electron cooling due to the synchrotron self-Compton is incorporated through the Y parameter (see, e.g. Panaiteescu & Kumar 2000; Sari & Esin 2001; Zhang & Mészáros 2001b).

The random thermal energy in a certain region is an essential parameter in calculating the synchrotron spectrum and the lightcurves. In stages 1 and 2, the only emitting site is the region heated by the shock (A). Starting from the stage 3, the emission sites increase to a total number of three, corresponding to the three shocks (although the shocks (B) and (C) die out in the stages 5 and 4, respectively). When the shocks are on, the random Lorentz factors at the shocks (A) and (C) are essentially the Lorentz factor of the shocks, i.e.,  $\gamma_A = \gamma_3$ , and  $\gamma_C = \gamma_5$ . For the shock (B), since the unshocked region (region 3) is also hot, the random Lorentz factor is not simply  $\gamma_{43}$ , but is rather  $\gamma_B = e_4/n_4 m_p c^2$ . When the shocks (B) and (C) die out, the random Lorentz factors in the relevant regions are still defined as  $\gamma_B = e_4/n_4 m_p c^2$  and  $\gamma_C = e_5/n_5 m_p c^2$ , which evolve adiabatically as discussed in §3.3.4 and §3.3.5. To calculate the synchrotron emission, we assume uniform values of the equipartition factors, i.e.,  $\epsilon_B$  and  $\epsilon_e$ , as well as the same electron power law index  $p$  in the three shock-heated regions. This is a crude approximation, but it is the simplest case which allows a straightforward comparison of the relative importance of the three shocks. The magnetic field in the region  $i$  is then  $B_i = (8\pi\epsilon_B e_i)^{1/2}$ . Assuming that the injection factor of the electrons is unity, the characteristic injected electron Lorentz factor is then  $\gamma_{m,X} = \epsilon_e[(p-2)/(p-1)](m_p/m_e)\gamma_X$ , where  $\gamma_X$  is the random Lorentz factor at the region X (A, B or C),  $m_p/m_e$  is the proton-electron mass ratio. Cooling frequencies are determined from the cooling electron energy, which is defined by the equality between the comoving time and the electron radiative cooling time. For the regions where the shocks are on and keep accelerating electrons, the synchrotron emission spectrum is calculated according to the four-segment broken power law description (Sari, Piran & Narayan 1998). For those regions where no new electrons are accelerated (region 5 in the stages 4 and 5, and region 4 in the stage 5), the synchrotron spectrum is modified by a sharp cut-off above the cooling frequency (although strictly speaking the cut-off should be exponential).

One crucial point in calculating the lightcurves is that the radiation from the three shocks which is emitted at the same fixed-frame time will reach the observer at different observer times. The main reason is that the region (4+5) usually moves faster (with  $\gamma_4$ ) than the region (2+3) (with  $\gamma_3$ ), so that for a same time interval in the fixed frame,  $dt$ , the emission from the sites heated by the shocks (B) and (C) reaches the observer (apart from the cosmological time dilation effect) in an interval of  $\sim dt/\gamma_4^2$ ,

while the emission from the shock (A) reaches the observer in an interval of  $\sim dt/\gamma_3^2$ . In our calculations, this effect is taken into account approximately. Defining the observer's time when the front of shell 3 reaches  $R_{sh}$  to be  $T_{sh}$ , we can approximate the observer's times corresponding to the regions (4+5) and (2+3) after  $T_{sh}$  to be roughly  $T_4 \sim T_{sh} + (R - R_{sh})/4\gamma_4^2 c$ , and  $T_3 \sim T_{sh} + (R - R_{sh})/4\gamma_3^2 c$ , respectively<sup>4</sup>. We see that the two times are different in the stages 3 and 4, but are the same in stages 1, 2 and 5. The overall effect of this correction is to "squeeze" the lightcurve signal from the fast moving region (4+5) during stages 3 and 4.

An example of a shell collision is presented in Figure 4. In Fig.4a, we plot the Lorentz factor evolution of various shocks and regions with respect to the blastwave radius, or equivalently the fixed-frame time  $t \sim R/c$ . This allows a clear assessment of the five stages analyzed in §3.3. Figure 4b presents an indicative optical lightcurve, identifying the contributions from the three emitting sites. The final lightcurve is complicated, with a few features which are caused by different emission sites. To make more sense of this numerical lightcurve, it is helpful to perform some further analysis. The emission component from the site related to the shock (A) is a standard "low frequency" lightcurve (Sari et al. 1998), except for a gentle flattening around  $10^4$  s, which corresponds to the relaxation boosting-up of  $\gamma_3$  in the stage 4 (Fig.4a). The emission components corresponding to the shocks (B) and (C) are more complicated. The lightcurve slopes in various sections depend on the (observer's) time dependence of the characteristic frequency,  $\nu_m \propto \gamma_i \gamma_X^2 B'$  for slow-cooling (which is usually the case) and  $\nu_c$  for fast-cooling, and the peak spectral flux,  $F_{\nu,m} \propto n_i \gamma_i B' R^3$ . Here  $\gamma_i$  denotes the bulk Lorentz factors ( $\gamma_3$  or  $\gamma_4$ ) and  $\gamma_X$  denotes the random Lorentz factors ( $\gamma_A$ ,  $\gamma_B$ , and  $\gamma_C$ ). Any change of the scaling law (with respect to  $T$ ) of any parameter (e.g.,  $\gamma_X$ ,  $\gamma_i$ ,  $n_i$ ,  $B'$ ,  $R$ ) results in a break in the lightcurves, and the lightcurve slope also depends on the spectral segment in which the observing frequency lies. In the specific example presented in Fig.4b, the climbing-up segment in the lightcurve (C) and the flat segment in the lightcurve (B) correspond to the violent injection stage 3, but the timescale is squeezed due to the increase of  $\gamma_4$  with respect to  $\gamma_3$ . The later drop-offs in both lightcurves correspond to the relaxation stage. Finally, all three lightcurves enter the post-relaxation stage at a same observer's time. There could be more breaks within the same stage. For example, the break on the lightcurve (B) in the post-relaxation stage is due to the transition from the (1/3) spectral segment to  $[-(p-1)/2]$  spectral segment. Two remarks can be made here. First, although in the stage 5 all the three random Lorentz factors decay as  $\propto R^{-3/2}$ , the lightcurve slopes on (B) and (C) in the  $[-(p-1)/2]$  spectral segment are steeper than the slope on (A) in the same spectral segment. This arises from the different scaling law in  $F_{\nu,m}$ , more particularly in  $n$ . For adiabatic expansion in the regions (B) and (C),  $n_i \propto (V')^{-1} \propto R^{-3} \gamma_i \propto R^{-9/2} \propto T^{-9/8}$ . In the region (A),  $n_2 \propto \gamma_3 \propto R^{-3/2} \propto T^{-3/8}$ . The lightcurve slopes for (B) and (C) then steepen by 0.75 relative to that

<sup>4</sup>Strictly speaking, since the region (4+5) trails behind the region (2+3), the time delay due to the emission from the region (4+5) crossing the shell 3 ought to be taken into account. Since the shell width  $\Delta_3 \ll R$ , this effect may be neglected as long as  $(R - R_{sh}) \gg \Delta_3$ .

of (A)<sup>5</sup>. Also the whole lightcurves (B) and (C) during the stage 5 also tilt by 0.75, which explains why the crossing of  $\nu_m$  in the lightcurve (B) looks a little unfamiliar. Second, although the random Lorentz factor in the site (B) is much higher than those in sites (A) and (C), the flux level is not, mainly because the density  $n_4$  is smaller than  $n_2$  and  $n_5$  during the violent collision process.

From Fig.4b, one can see that the injection signatures of a violent collision are rather complicated. There could be more than one signature which may be related to different emission sites. This gives rise to a whole set of injection patterns. For example, the sharp decline of the site (C) emission in the relaxation stage, given an appropriate set of parameters, could be an explanation for the ROTSE prompt optical flash observation in GRB 990123, which is conventionally interpreted as the cooling from the reverse-shock-heated region in an impulsive shell case (Mészáros & Rees 1997a, 1999; Sari & Piran 1999, Kobayashi 2000). The modest sticking-out of the optical lightcurve (B) around several  $10^5$  s (Fig.4a) seems to have been observed in some GRB lightcurves, although the chromatic nature of this rise rules it out as a possible explanation of the achromatic bump observed in GRB 000301C, which can be interpreted as a gravitational micro-lensing event (Garnavich et al. 2000).

The main characteristic which can be used to differentiate a post-injection model from other possible mechanisms leading to bumps in the light curve is the broad-band behavior. Since the injection processes produce global dynamics changes, they will leave imprints at all wavebands. In Figure 5 we present the broad-band injection lightcurves for (a) a violent injection; (b) a mild injection throughout. We can see that the mild injection case is similar to the Poynting-flux-dominated injection case (Fig.1), as has been discussed in §3.3.2. The violent injection case shows rather different and complex behaviors. The rising times in various bands are essentially the same, but the bump shapes are quite different, mainly because different shocks contribute differently in different bands.

#### 4. SUMMARY & DISCUSSION

In this paper, we have analyzed the observational consequences of a GRB fireball which receives an additional energy injection from the central engine during the afterglow phase. We have discussed the cases where the injection is either a continuous Poynting-flux-dominated wind, or a kinetic-energy-dominated matter shell. For the latter, we discuss the cases when the collision is either “mild” or “violent”, distinguished by whether additional shocks persist and additional emission sites arise in the outflow. We reach the following general conclusions:

1. A post-burst injection energy  $E_{\text{inj}} \sim E_{\text{imp}}$  is generally required to cause a noticeable signature in the afterglow lightcurves. This is especially so for the Poynting flux injection case and for the mild kinetic energy injection case. For a violent collision, a faster rear shell (i.e.  $\gamma_6 \gg \gamma_3$ ) can compensate for a lower rear shell total energy (Fig.3).

2. For the kinetic-energy injection case, we have explicitly studied the three-shell interaction process, described by a set of equations (eqs.[5]-[8]). We find that the forma-

tion of an additional pair of shocks from the collision of two shells is not as common as usually thought. Depending on the status of the rear shell when the collision occurs (spreading or not), a minimum relative speed between the two colliding shells is required, as shown in Figure 3. In many cases, such as expected in the internal shock model where slow trailing shells catch up with the fast shells when the latter are decelerated, the relative speed between the shells are usually not high enough, and the injections are likely to be mild. We expect that a violent injection most likely arises from a late injection of a high entropy shell from the central engine. Since the baryon loading at late times is expected to be smaller than that at earlier times, this is not unusual given a long-lived erratic central engine.

3. If no additional emission sites form during the injection, such as the case of the Poynting-flux-dominated flow, the injection signature is usually very gradual (Fig.1 and Fig.5b). In the case of a violent injection, the signatures are complicated and some could be very abrupt. In either case, the final Lorentz factor of the blastwave, as well as the emission flux level, are boosted up with respect to the case without post-injection.

4. A prominent characteristic of the post-injection process is the conspiratorial variation of the flux in all bands (Fig.1 and Fig.5), due to the changes in the dynamics of the emitting region. This provides a strong criterion for judging whether a bump signature is due to an injection or to other reasons. For example, the supernova component (Bloom et al. 1999; Reichart 1999; Galama et al. 2000) and the dust echo (Esin & Blandford 2000) interpretations do not predict prominent changes in X-ray and radio lightcurves. The gravitational micro-lensing model may be more difficult to differentiate from a post-injection event, since it is essentially an achromatic feature, although it can have some chromatic features (Granot & Loeb 2001). The Poynting-flow injection case is also achromatic. The differentiation between the two possibilities can be only based on the shape of the bump. For example, the micro-lensing model predicts a more abrupt (shorter duration) feature than does the Poynting-injection. Another feature of micro-lensing is that the afterglow lightcurve will resume the level of no magnification when the lensing event ends, while in the injection case, the global energetics is always boosted up. Prospects of differentiation look better for a violent matter-injection case, in which the bumps in different bands have quite different shapes, although the rising time is essentially the same (Fig.5a). Overall, future broadband afterglow data with very good temporal coverages plus a more detailed modelling can in principle differentiate the injection signature from the other possibilities. Within the injection itself, different injection signatures may provide direct information about the nature of the injection, and possibly, also about the nature of the central engine.

The treatment presented in this paper is generic and applicable also to more complicated injection processes. For example, for multi-shell-collision cases, one simply needs to regard the emitting gas after each injection as a new “impulsive” component, and a newly injected shell or wind can be treated in the same way. Since collisions in the internal shock scenario also involve a similar process (but

<sup>5</sup>In Fig.4b, the steepening is slightly smaller than 0.75. This is because the lightcurve (A) is in the  $(-p/2)$  spectral regime, which has steepened by itself.

without the interaction with the ISM), the treatment presented here may be also usable in studying GRB gamma-ray lightcurves in the prompt phase. The shell merging is a very complicated process, and here we have used some approximations leading to a semi-analytic description of the whole process. For example, we have assumed that the decelerating shell has a uniform density and speed, while a more accurate treatment ought to take into account the Blandford-McKee (1976) self-similar profiles. This approximation nonetheless provides a first-order treatment to the problem. Another assumption we have made is that the total internal energy in each region is solely due to the shock heating. Strictly speaking, adiabatic loss due to expansion should be taken into account (e.g. Panaitescu et al. 1998). However, as long as shock heating is going on, the adiabatic loss is not important. Only when shock heating ceases (e.g., region 5 in the stages 4 and 5, and region 4 in the stage 5), do we consider the adiabatic loss. Furthermore, in all our calculations, the effects concerning spreading in the photon arrival time due to the curvature of the shells as well as their non-zero thicknesses have been ignored. These effects are essential in more detailed afterglow modeling (e.g. Granot, Piran & Sari 1999), which tend to smear out features on the lightcurves. With these effects taken into account, we expect that the sharp features shown in Fig.5a ought to be smeared out.

Finally we compare our results with the previous relevant treatments. Rees & Mészáros (1998), and Panaitescu et al. (1998) have discussed the “refreshed” injection scenario in which all the mini-shells are assumed to be ejected simultaneously, but with a power-law distribution of  $\Gamma$ . Al-

though such a scenario is of interest and can be modeled relatively easily, it is unclear whether it is a closer representation of reality. The Poynting-flux-dominated injection within the pulsar central engine model has been discussed earlier by Dai & Lu (1998), but their indicative lightcurve was too abrupt. Their recent treatments (Dai & Lu 2001; Wang & Dai 2001) generally agree with the gradual evolution picture obtained in this paper. For the shell collision injection case, the most relevant precedent discussion is the one by Kumar & Piran (2000). Although our results generally agree with theirs on, e.g., the hydrodynamic treatments, our shock forming condition (Fig.3) is more demanding than theirs. In fact, for the specific example they presented, i.e.,  $E_{0,6} \sim E_{0,3}$ , and  $\gamma_{36} \sim 1.25$ , the injection is only mild according to our criterion, while they argue that two shocks will form and propagate into the two shells. This discrepancy may be due to their not having included the hydrodynamics of the three-shell interaction. They also presented an indicative injection lightcurve (their Fig.5). However, this lightcurve is more analogous to our mild-injection signature (Fig.5b). As discussed in §3.4, a violent injection tends to generate a more complicated lightcurve with possibly more than one signature, as indicated in Fig.4b and Fig.5a.

We are grateful to Pawan Kumar, Alin Panaitescu and Re’em Sari for informative correspondence and Oleg Karagaltsev for discussions, to the referee for a detailed and helpful report, and to NASA NAG5-9192 and NAG5-9153 for support.

## REFERENCES

Blackman, E. G., & Yi, I. 1998, *ApJ*, 498, L31  
 Blandford, R., & McKee, C. 1976, *Phys. Fluids*, 19, 1130  
 Bloom, J. S. et al. 1999, *Nature*, 401, 453  
 Chiang, J., & Dermer, C. D. 1999, *ApJ*, 512, 699  
 Dai, Z. G., & Lu, T. 1998, *Phys. Rev. Lett.*, 81, 4301  
 —. 2001, *A&A*, 367, 501  
 Esin, A. A., & Blandford, R. 2000, *ApJ*, 534, L151  
 Galama, T. et al. 2000, *ApJ*, 536, 185  
 Garnavich, P., Loeb, A., & Stanek, K. 2000, *ApJ*, 544, L11  
 Granot, J., & Loeb, A. 2001, *ApJ*, 551, L63  
 Granot, J., Piran, T., & Sari, R. 1999, *ApJ*, 513, 679  
 Huang, Y. F., Dai, Z. G., & Lu, T. 1999, *MNRAS*, 309, 513  
 Kennel, C. F., & Coroniti, F. V. 1984, *ApJ*, 283, 694  
 Kobayashi, S. 2000, *ApJ*, 545, 807  
 Kobayashi, S., Piran, T. & Sari, R. 1999, *ApJ*, 513, 669  
 Kumar, P., & Piran, T. 2000, *ApJ*, 532, 286  
 Lyutikov, M., & Blackman, E. G. 2001, *MNRAS*, 321, 177  
 Mészáros, P., Laguna, P. & Rees, M.J. 1993, *ApJ*, 415, 181  
 Mészáros, P., & Rees, M. J. 1997a, *ApJ*, 476, 232  
 —. 1997b, *ApJ*, 482, L29  
 —. 1999, *MNRAS*, 306, L39  
 Panaitescu, A., & Kumar, P. 2000, *ApJ*, 543, 66  
 Panaitescu, A., Mészáros, P., & Rees, M. J. 1998, *ApJ*, 503, 314  
 Piran, T. 1999, *Phys. Rep.*, 314, 575  
 Piran, T., Shemi, A., & Narayan, R. 1993, *MNRAS*, 263, 861  
 Rees, M. J. & Mészáros, P. 1998, *ApJ*, 496, L1  
 Reichart, D.E. 1999, *ApJ*, 521, L111  
 Sari, R., & Esin, A. A. 2001, *ApJ*, 548, 787  
 Sari, R., & Piran, T. 1995, *ApJ*, 455, L143  
 —. 1999, *ApJ*, 517, L109  
 Sari, R., Piran, T., & Narayan, R. 1998, *ApJ*, 497, L17  
 Spruit, H. C., Daigne, F., & Drenkhahn, G. 2001, *A&A*, 369, 694  
 Usov, V. V. 1994, *MNRAS*, 267, 1035  
 —. 1999, in *ASP Conf. Ser.* 190, *Gamma-Ray Bursts: The First Three Minutes*, ed. J. Poutanen & R. Svensson (San Francisco: ASP), 153  
 Wang, W. & Dai, Z.G. 2001, *Chin. Phys. Lett.*, 18, 1153  
 Zhang, B., & Mészáros, P. 2001a, *ApJ*, 552, L35  
 —. 2001b, *ApJ*, 559, 110